Supporting Information

Confining High-Entropy Alloys within MOF-Derived Architectures:

A Dual-Site Strategy Boosting Photothermal CO_2 Methanation

Chunlin Ke[1], Siyu Song[1], Shenghao Li[1], Fengliang Wang[2], Ruiqi Fang[2],

Xin Zhao[2], Chao Wang[1*]

1. Guangdong Provincial Key Laboratory on Functional Soft Condensed Matter, School of Materials and Energy, Guangdong University of Technology, Guangzhou 510006, China

2. School of Chemistry and Chemical Engineering, South China University of Technology, Guangzhou 510640, Guangdong, China

* Corresponding author. (C. Wang) E-mail address: chaowang@gdut.edu.cn;

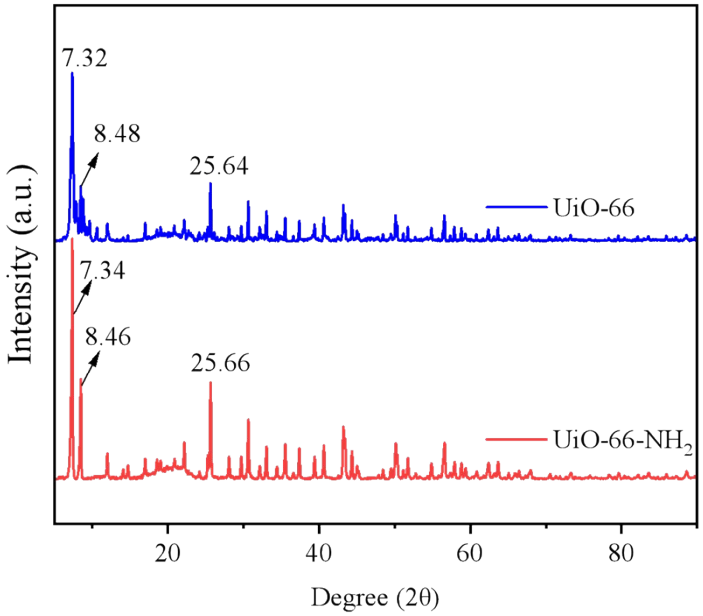

Fig S1. XRD patterns of UiO-66 and UiO-66-NH_2.

The characteristic diffraction peaks are precisely situated at $2\theta = 7.32°$, 8.48°, and 25.64°, which match perfectly with JCPDS standard card No. 00-056-1048. No impurity peaks are detected, verifying the excellent crystallinity and pure phase of UiO-66.[1] The positions of the characteristic diffraction peaks almost coincide with those of UiO-66-NH_2 ($2\theta = 7.34°$, 8.46°, 25.66°, etc.). Only slight lattice distortion is caused by the amino-substituted terephthalic acid ligand, giving rise to a peak shift of less than 0.2° for some signals. This is fully consistent with the reported XRD patterns of amino-functionalized UiO-66-NH_2, confirming the successful incorporation of amino groups without damaging the main framework of UiO-66.[2]

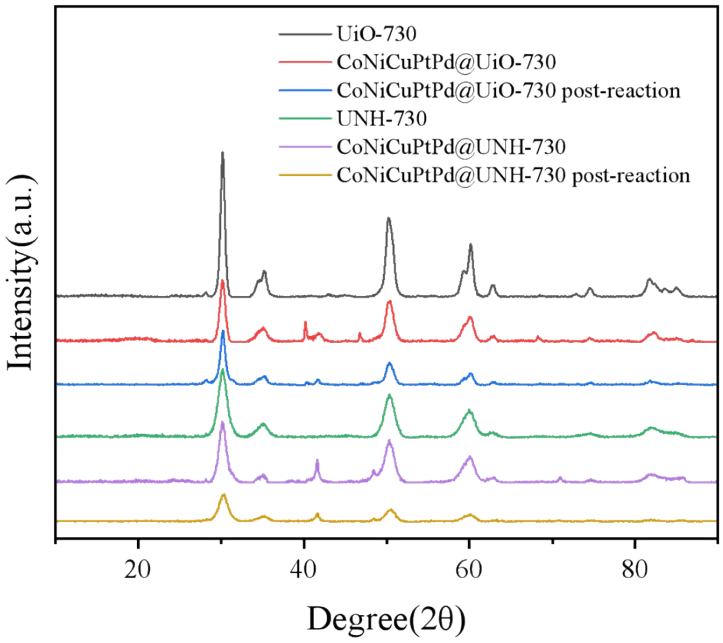

Fig S2. XRD patterns of UiO-730, UNH-730, CoNiCuPtPd@UiO-730, and CoNiCuPtPd@UNH-730

The post-reaction XRD pattern shown in Fig S2 reveals no shift in the characteristic peak positions of the HEA (2θ = 41.7°, 48.4°, etc.). The characteristic peaks of t-ZrO_2 (2θ = 30.2°, 35.1°, etc.) show no attenuation or peak shift, and no impurity phases (e.g., metal oxides, carbides) are detected. The absence of the broad peak for amorphous carbon confirms no carbon deposition.

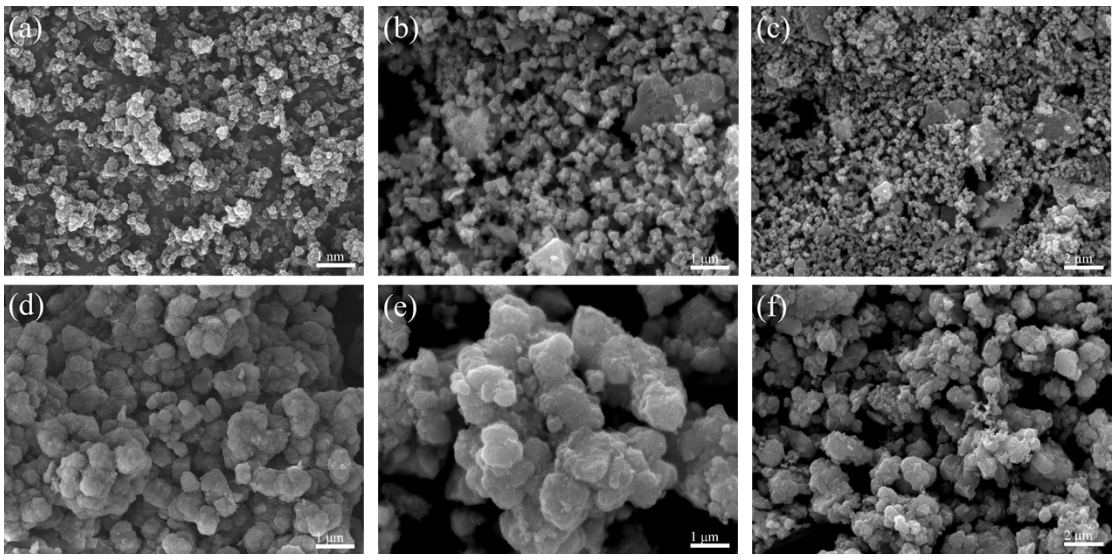

Fig S3. SEM images of (a) UiO-66, (d) UiO-66-NH_2, (b) pyrolyzed UiO-730, (e) pyrolyzed UNH-730, (c) spent CoNiCuPtPd@UiO-730, and (f) spent CoNiCuPtPd@UNH-730.

The SEM image of UiO-66 (Fig S3a) presents a regular octahedral bulk structure with uniform particle size, consistent with the typical morphological features of UiO-66. The SEM image of UiO-66-NH_2 (Fig S3d) also shows a regular octahedral structure with slightly smaller particles than UiO-66, which is ascribed to the electron effect of amino groups that accelerates the nucleation process of the MOF. The SEM images of UiO-730 (pyrolyzed UiO-66, Fig S3b) and UNH-730 (pyrolyzed UiO-66-NH_2, Fig S3e) illustrate that both materials preserve the basic morphology of the MOF after pyrolysis. As revealed by the post-reaction SEM images of CoNiCuPtPd@UiO-730 (Fig S3c) and CoNiCuPtPd@UNH-730 (Fig S3f), both samples maintain the porous bulk morphology inherited from the MOF precursor after reaction, with no obvious cracking, fragmentation or sintering.

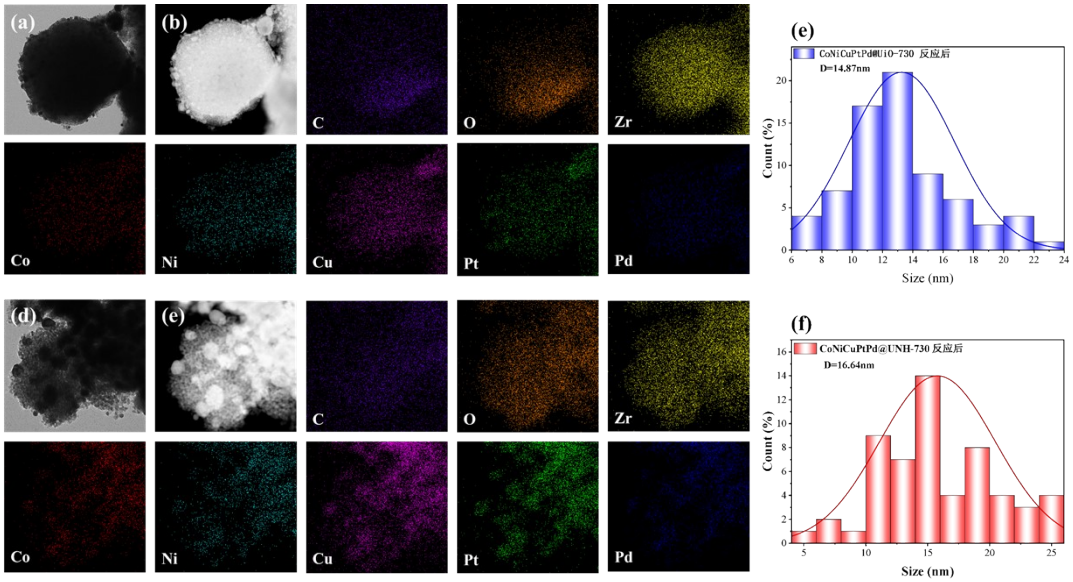

Fig S4. (a) TEM image of UiO-66 after reaction; (b) TEM image and EDS elemental mapping images of CoNiCuPtPd@UiO-730 after reaction; (c) Particle size distribution diagram of CoNiCuPtPd@UiO-730 after reaction; (d) TEM image of UiO-66-NH_2 after reaction; (e) TEM image and EDS elemental mapping images of CoNiCuPtPd@UNH-730 after reaction; (f) Particle size distribution diagram of CoNiCuPtPd@UNH-730 after reaction.

The supports of the spent CoNiCuPtPd@UiO-730 and CoNiCuPtPd@UNH-730 still retain the UiO-66-derived ZrO_2/carbon composite structure. In spent CoNiCuPtPd@UiO-730, the Co, Ni, Pt, Pd, and Cu elements show obvious local segregation, with the signal of individual metals concentrated in local regions and no homogeneous distribution across the whole catalyst. In contrast, the five metal elements (Co, Ni, Cu, Pt, and Pd) in spent CoNiCuPtPd@UNH-730 are uniformly distributed throughout the sample without distinct segregation, verifying that the single-phase high-entropy alloy (HEA) structure is well preserved after the reaction.

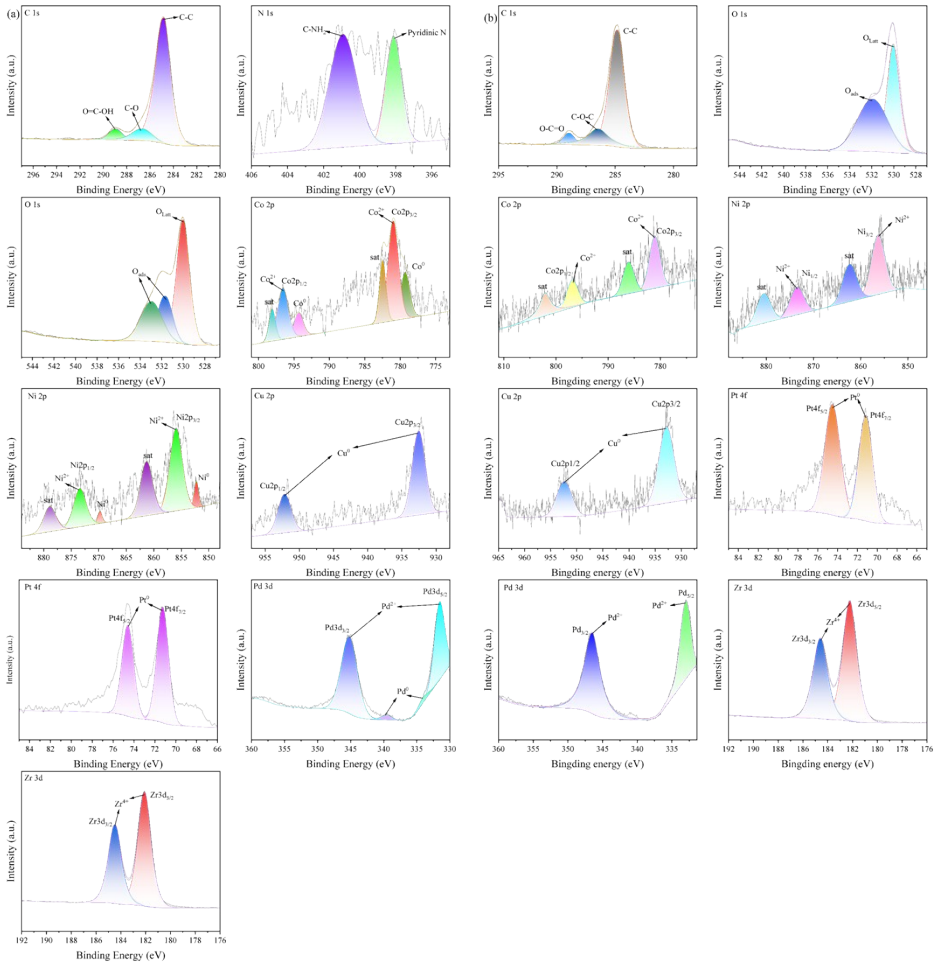

Fig S5. XPS spectra of (a) spent CoNiCuPtPd@UNH-730 and (b) spent CoNiCuPtPd@UiO-730

As shown in FigS5 (a), Co^0, Ni^0, Cu^0, Pt^0, and Pd^0 remain the dominant valence states in the spent CoNiCuPtPd@UNH-730 with no obvious peak shift. The intensity of the N 1s peak at 397-398 eV shows no attenuation, confirming the structural stability of pyridinic N sites derived from amino-group pyrolysis. The surface-adsorbed oxygen peak at 530.58 eV in the O 1s spectrum remains unchanged, indicating a stable oxygen vacancy concentration. As shown in FigS5 (b), the post-reaction XPS of CoNiCuPtPd@UiO-730 exhibits enhanced peaks for oxidized metal species. For both

samples, the Zr binding energy (≈182.6 eV) is consistent with that of the fresh catalysts. The C-C peak at 284.8 eV in the C 1s spectrum, originating from the pyrolyzed carbon framework, shows little change in intensity, demonstrating that the ZrO_2/carbon support structure remains stable after reaction.

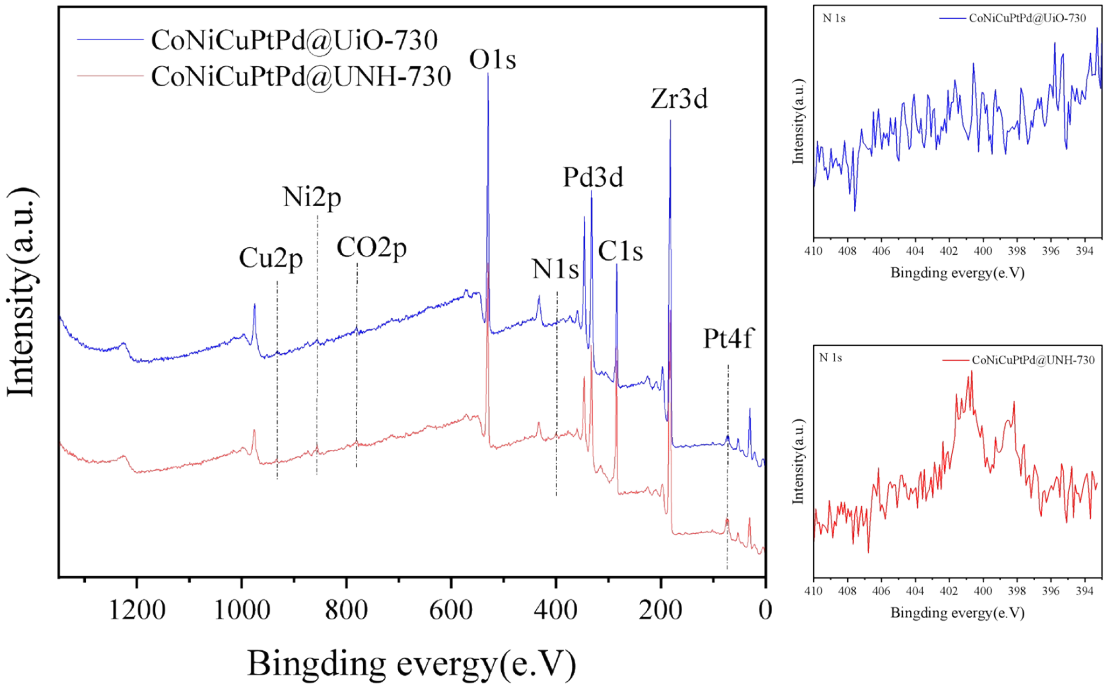

Fig S6. Full-range and N 1s X-ray photoelectron spectroscopy (XPS) spectra of CoNiCuPtPd@UiO-730 and CoNiCuPtPd@UNH-730

CoNiCuPtPd@UiO-730 (the N-free reference) shows no obvious characteristic peak in the N 1s region, only a weak background signal without resolvable components. This confirms that the UiO-66 precursor contains no amino groups and no nitrogen was introduced into the support after pyrolysis, ruling out nitrogen contamination. For CoNiCuPtPd@UNH-730 (the N-doped sample), two well-resolved peaks are obtained after peak fitting. The peak at 397.8 eV is assigned to pyridinic N, in agreement with

our previous analysis, which corresponds to the sites coordinated with metal ions or pyridine rings formed by amino-group pyrolysis. The peak at 399.9 eV is attributed to C-N bonds, originating from the nitrogen-doped structure formed by the combination of amino groups and the carbon framework.

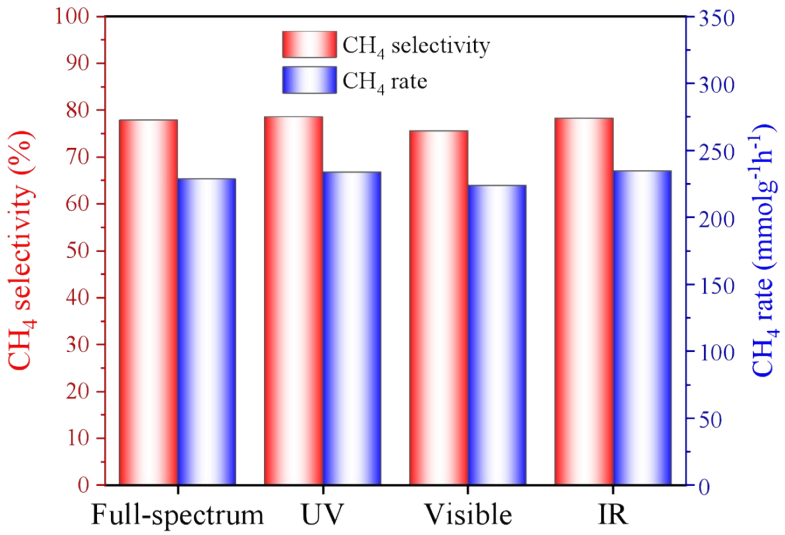

Fig S7. CH_4 rate and selectivity under full-spectrum, ultraviolet, visible, and near-infrared irradiation.

The CH_4 rate and selectivity under the three wavelength bands show no significant difference from those under full-spectrum irradiation. This indirectly confirms that the catalytic process in this work is a pure thermal effect. The catalytic performance is determined solely by temperature, independent of light wavelength, and light serves only as a heating source.

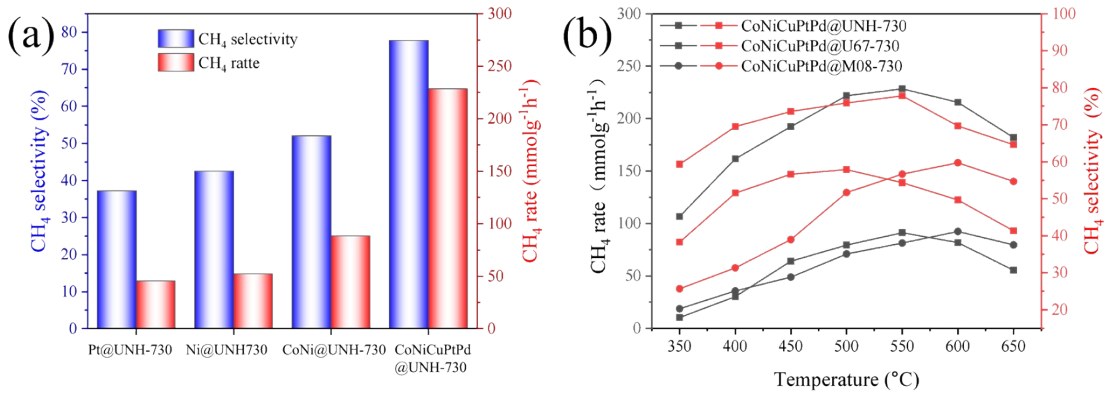

Fig S8. (a) Performance comparison of Pt@UNH-730, Ni@UNH-730, CoNi@UNH-730 and CoNiCuPtPd@UNH-730. (b) CO_2 methanation performance comparison of CoNiCuPtPd@U67-730, CoNiCuPtPd@M08-730 and CoNiCuPtPd@UNH-730.

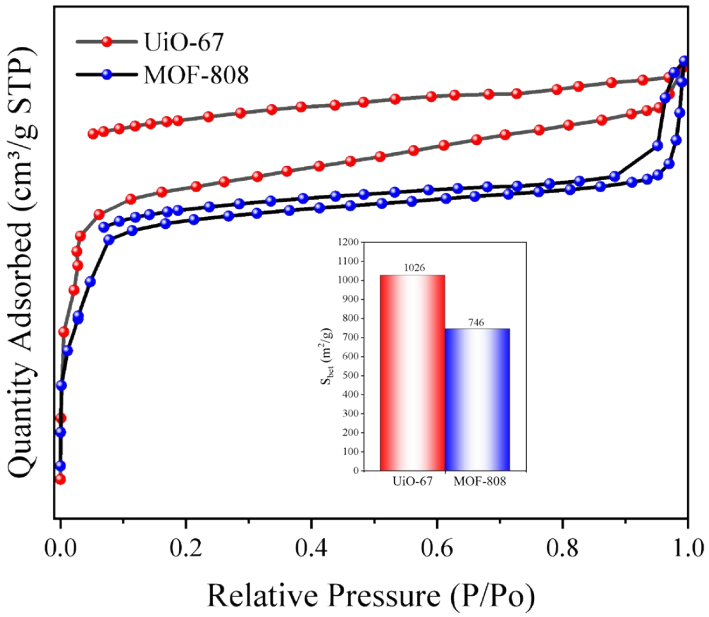

Fig S9. N_2 adsorption-desorption isotherms of UiO-67, MOF-808.

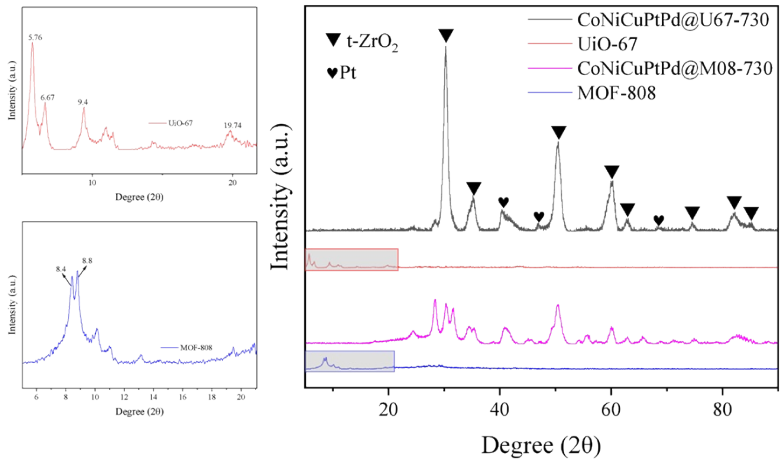

Fig S10. XRD patterns of UiO-67, MOF-808, CoNiCuPtPd@U67-730 and CoNiCuPtPd@M08-730.

Characteristic diffraction peaks at 2θ = 5.76°, 6.66°, 9.4°, and 19.74° correspond precisely to the (111), (200), (220), and (600) planes, assigned to UiO-67.[3] Peaks at 2θ = 8.4° and 8.8° match well with the (311) and (222) planes, characteristic of MOF-808.[4] After pyrolysis, loading and reduction, diffraction peaks of metallic Pt and ZrO_2 appeared in CoNiCuPtPd@U67-730, while only ZrO_2 peaks were detected in CoNiCuPtPd@M08-730. No single solid-solution phase of CoNiCuPtPd was formed in either sample.

Table S1. Catalytic activity for CH_4 production via photo-thermal route in the reported literature.

Catalysts	Surface temperature (°C)	CH_4 Rate（mmol $g^{-1}h^{-1}$）	CH_4 selectivity (%)	Ref
CoNiCuPtPd@UNH	550°C	228.36	77.8	This work
0.35%Ru@$Ni_2V_2O_7$	350°C	114.9	99	5
15Ni/CeO_2-U	200°C	204	98.7	6
Ni/$CeNiO_3$	250°C	163.7	93.1	7
TiO_2-x/Ni-550	700°C	180	99	8
Co@CN-700	250°C	199.4	99.4	9
Ni@TiO_2	469°C	286.5	81.8	10
CoNiCuRuPd HEA	400°C	137	68.3	11
FeNiCrMnCo alloy	290°C	199	93	12

The rate and selectivity of CH_4 were calculated based on the following equations, respectively:

$$R_{ch4} = \frac{n_{CH4}}{weight\ of\ catalyst} \times 60 \quad (1)$$

$$S_{ch4} = \frac{n_{CH4}}{n_{CH4} + n_{CO}} \times 100\% \quad (2)$$

$$n_{CH4} = \frac{F \times [CH_4]}{22.4} \quad (3)$$

$$n_{CO} = \frac{F \times [CO]}{22.4} \quad (4)$$

Here, F represents the gas flow rate (mL min^{-1}). $[CH_4]$ and [CO] are the respective concentrations (vol.%) of CH_4 and CO detected by online GC.

References

[1] Wang, H. Li, Q. Chen, J. Jia, H. Journal of Materials Chemistry A, 2024, 12(26), 15803-15813.

[2] Kandiah, M. Nilsen, M. H. Usseglio, S. Jakobsen, S. Olsbye, U. Tilset, M. Lillerud, K. P. Chemistry of Materials, 2010, 22(24), 6632-6640.

[3] Almotiry, S. Alhogbi, B. G. Abdel Salam, M. Jaremko, M. Catalysts, 2024, 14(9), 573.

[4] Roa, V. Cea, S. Pazo, C. Llanos, J. Olivares, D. Escalona, N. Schott, E. Dalton Transactions, 2025, 54(25), 10085-10096.

[5] Chen, Y. Zhang, Y. Fan, G. Song, L. Jia, G. Huang, H. Zou, Z. Joule, 2021, 5(12), 3235-3251.

[6] Li, Y. Yang, Y. Huang, Z. Zhou, H. Zeng, R. Lin, X. Zhang, Z. Chemical Engineering Journal, 2025, 511, 162073.

[7] Tian, W. Wang, N. Yan, W. Fu, R. Li, T. Yu, F. Catalysis Science & Technology

2026.

[8] Zhang, C. Zhang, J. Che, L. Wang, X. Shi, L. Applied Catalysis A: General, 2025, 120613.

[9] Xia, Z. Zhai, J. Lin, L. Chen, X. Xue, C. Jia, S. Han, B. Chemical Science, 2025, 16, 13382-13389.

[10] Ma, J. Liu, T. Chen, G. Liu, S. Gong, W. Bai, Y. Xiong, Y. Applied Catalysis B: Environment and Energy, 2024, 344, 123600.

[11] Mori, K. Hashimoto, N. Kamiuchi, N. Yoshida, H. Kobayashi, H. Yamashita, H. Nature communications, 2021, 12(1), 3884.

[12] Li, J. Ren, W. Wei, B. Teng, Y. Wang, W. Wang, L. Liu, Q. Science China Materials, 2025, 1-27.